EVALUATION OF STRONG MOTIONS CAUSED BY THE 2022 PAKTIKA EARTHQUAKE OF AFGHANISTAN BY ENPIRICAL AND FINITE ELEMENT METHODS AND FAULT RUPTURE MODELING TECHNIQUE BASED ON EVOLUTIONARY POWER SPECTRUM

A. Bari Jaheed[1], Ömer Aydan[2], Takashi ITO[3], Naoki IWATA[4] and Takaaki IKEDA[5]

[1]Graduate Student, Dept. of Civil Eng. and Architechture, University of Ryukyus
(1Senbaru, Nishihara, Okinawa, 903-0213, Japan)
E-mail: bari.jahed@gmail.com
[2]Member of JSCE, Emeritus Professor, Dept. of Civil Eng. and Architechture, University of Ryukyus
(1 Senbaru, Nishihara, Okinawa, 903-0213, Japan)
E-mail: aydan@tec.u-ryukyu.ac.jp
[3]Member of JSCE, Professor, Dept. of Civil Eng. and Architechture, University of Ryukyus
(1 Senbaru, Nishihara, Okinawa, 903-0213, Japan)
E-mail: takito@tec.u-ryukyu.ac.jp
[4]Member of JSCE, Nuclear project dept., Chuden Engineering Consultants
(2-3-30 Deshio, Minami-ku, Hiroshima, 734-8510, Japan)
E-mail: n.iwata@cecnet.co.jp
[5]Member of JSCE, Professor, Dept., Civil and Environmental Engineering, Nagoka University of Technology
(1603-1 Kamitomioka Nagaoka. 940-2188, Japan)
E-mail: ikeda@vos.nagaokaut.ac.jp

The 2022 Paktika earthquake with a moment magnitude of 6.2 occurred on June 22, 2022 in the Khost Province of Afghanistan. This study is concerned with the evaluation of strong motions caused by the Paktika earthquake by utilizing empirical methods, finite element method and empirical green function method. The evaluations and estimations of maximum ground acceleration, velocity and permanent ground deformations are compared with each other as well as those inferred from the failure of some simple structures in Spera and Gayan Districts. The evaluations and comparisons of strong motions are presented and their implications on the seismic damage are discussed.

Key Words : *Paktika earthquake, strong motion, empirical method, FEM, SAR*

1. INTRODUCTION

The 2022 Paktika earthquake with a moment magnitude of 6.2 occurred at 1:24 local time on June 22, 2022 in the Khost Province of Afghanistan. Spera, Gayan and Barmal Districts were heavily damaged and more the casualty was more than 1000 people. The earthquake occurred within the India-Eurasian plate boundary zone and it is about 65-70 km far from the Chaman fault, which has a sinistral sense of deformation. However, the faulting mechanism of the 2022 Paktika earthquake was quite similar to the anticipated faulting mechanism of earthquakes along the Chaman fault. Despite the high seismicity activity of Afghanistan, the country is poorly instrumented due to the occupations of former Soviet Union and USA and internal wars for decades. Therefore, there was no strong motion record related to the Paktika earthquake. The failure of some simple structures implies implies that the maximum ground acceleration and velocity could be more than 300 gals and 50 kines. Some satellite image analyses indicated that the slope failures were also widespread despite there are almost no reports of geotechnical failures. The authors concerned with the evaluation of strong motions

caused by the 2022 Paktika earthquake by utilizing empirical methods, finite element method and sub-fault rupture modelling with evolutionary power spectrum. The evaluations and estimations of maximum ground acceleration, velocity and permanent ground deformations obtained from various methods are compared with each other as well as those inferred from the failure of some simple structures in Spera and Gayan Districts. These evaluations and comparisons of strong motions are presented and discussed.

2. SEISMO-TECTONICS

Afghanistan is in Eurasian orogenic belt and one of the seismically active belts in the world. Modern fault movements, deformations, and earthquakes in Afghanistan are driven by the northward subduction of Indian and Arabian plates beneath Eurasia plate (**Fig.1**). The subduction of Arabian plate along Makran subduction zone and the intrusion of Indian plate into Eurasian plate resulted in some major tectonic structures in the region. The Chaman Fault System is said to be accommodating 200 km relative slip and caused some earthquakes greater than M7. The most recent event was 1935 Quetta earthquake. The subduction Arabian plate beneath Eurasian plate causes a relative slip between the Lut block in Iran and the Helmand/ Sistan block of Afghanistan, and it is called Sistan Suture zone. The seismo-tectonics of Kanadahar region is greatly affected by the relative slip along Chaman fault between Eurasian and Indo-Australian plate and

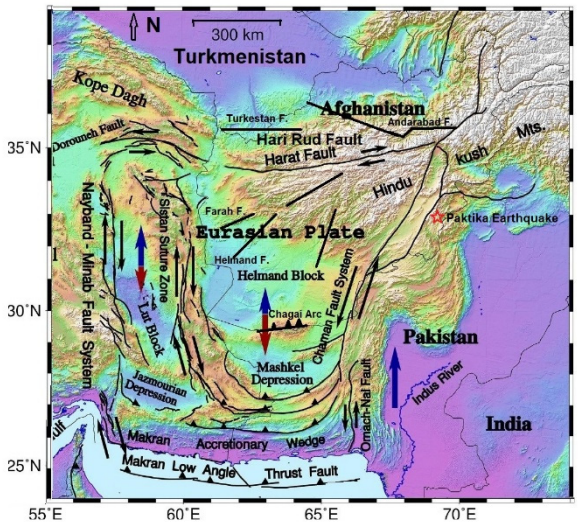

Fig.1 Tectonics of Afghanistan and neighboring countries (modified from Nemati[1]).

this slip is probably the main cause of folding and intrusions in the region.

The active faults within Afghanistan can be divided into 5 fault systems; namely, Chaman, Hari-rud (Herat) and Central Badakhshan fault systems and Helmand internal fault system and South Turkestan fault system (**Fig.1**).

In the southeastern Afghanistan and adjacent Pakistan, the Chaman fault system accommodates much of the differential movements between the Indian and Eurasian plates. The fault system has a reported slip rate of 2-20mm/year and higher where it enters western Pakistan. The Indian plate has a 20-40mm/year velocity where it comes close to a 300-400km segment of Chaman fault between (31°N-33.5°N), suggesting that M>7.0 could occur at 200 years interval in this location. In central Afghanistan, the Hari Rud (Herat) fault having dextral sense extends from north of Kabul westward to Iran border with a slip rate of 2mm/year, but evidence for active faulting remain controversial. In northeast Afghanistan, Badakshan and Dawraz-Karakul faults extends into in Pamir and Hindu Kush Mountains. Further north next to Turkmenistan and Uzbekistan, there are some faults such as Turkestan fault zone and Andarabad fault. Hindukush region of Afghanistan is seismically very active. The next seismically active regions are located along Chaman fault in east, Chagai Arc and Makran region in south and Sistan Suture Zone along Iran and Afghanistan Border in west. The north Afghanistan is also known to be very seismically active with earthquakes greater than M7.

3. CHARACTERISTICS OF MAIN SHOCK

The main shock of the 2022 Paktika earthquake occurred within the India-Eurasian plate boundary zone and it is about 65-70 km far from the east of the Chaman fault. Different institutes estimated the moment magnitude of the main shock ranging between 6.1 and 6.4. USGS[2] and Harvard CMT[3] estimated that the moment magnitude is 6.2 with local magnitude of 5.9 and surface wave magnitude of 5.9.

The focal plane solutions indicated that the earthquake was caused by a sinistral strike-slip fault. The fault has a dip direction of 294 degrees and dip angle of 87 degrees . The rake angle was 11 degrees implying a slight normal faulting. **Fig.2** shows the focal mechanism. The length and the maximum slip of the causative

earthquake fault were estimated to be between 15.9-20.0 km and 82-160 cm as given in **Table 1**.

4. PERMANENT GROUND DEFORMATIONS FROM DInSAR

Methods based on Synthetic Aperture Radar (SAR) and its derivatives such DInSAR have been commonly used to infer permanent ground deformations caused by earthquakes. The authors utilized the SAR images obtained from Sentinel-1 Satelite of European Space Agency.

The satellite orbits the Earth in a north-south direction and makes observations by radaring right downwards. Therefore, observations are made from the west for Ascending, which flies from south to north, and from the east for Descending, which flies from north to south. The SAR data obtained are the intensity and phase of the radar reflected waves from the ground surface. Observations using this SAR data are carried out two or more times at the same point on the earth's surface, and the phase difference of the reflected waves is calculated to obtain the surface displacement (LOS displacement) in the radar's line-of-sight (LOS) direction in areal terms using Differental Interferometric SAR (DInSAR) technique was used to assess the surface deformation.

The difference between 18 June and 30 June 2022 was calculated for Ascending, and the difference between 19 June and 1 July 2022 for Descending. **Figs.3** and **4** show the permanent deformation distribution (LOS) for Ascending and Descending orbits.

In Ascending in **Fig.4**, a LOS displacement in the direction closer to the satellite of +40 cm is observed on the south side of the epicentre of the upper plate. On the other hand, a LOS displacement in the direction away from the

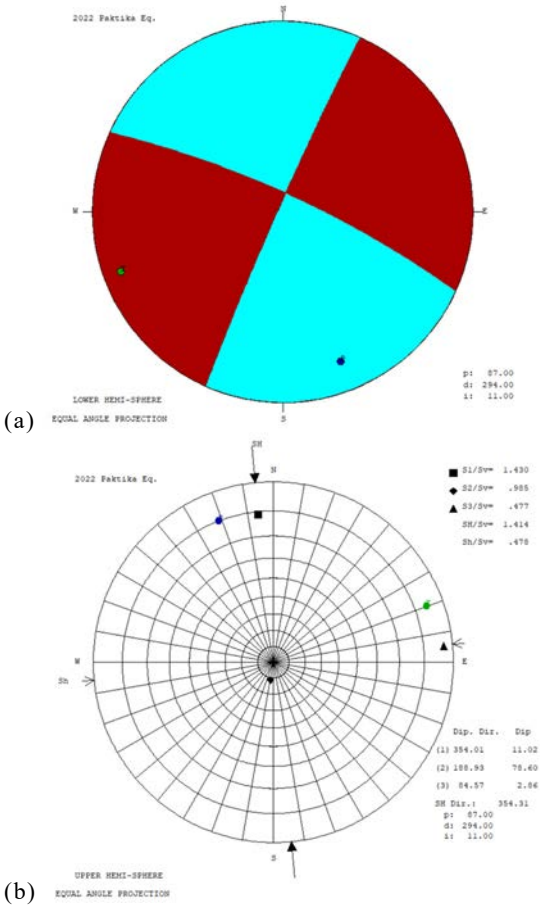

Fig.2 Focal mechanism and its inferred stress state.

Table 1 Seismic parameters of the main shock.

Institute	Mw	Length (km)	Max.Slip (cm)	Duration (seconds)
USGS	6.2	5.3x3=15.9	160	5.3
Harvard	6.2	6.2x3=18.6	-	6.2
Ö.A.	6.2	20	84 (42x2)	6.0

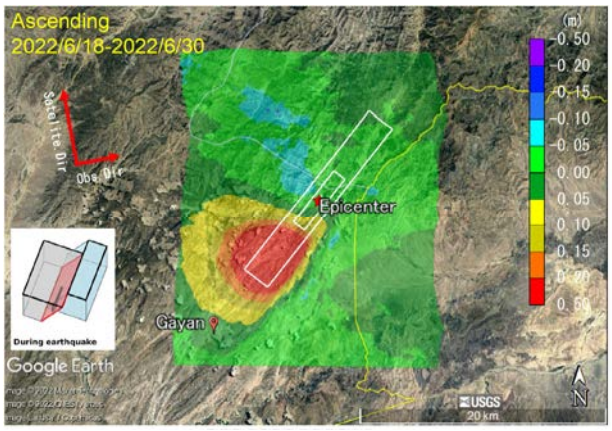

Fig.3 Permanent ground deformations (LOS) obtained from DInSAR for Ascending images.

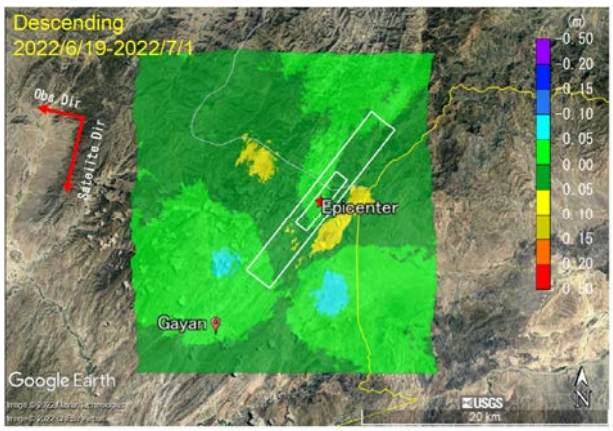

Fig.4 Permanent ground deformations obtained from DInSAR for Descending images.

satellite of -5 cm is observed at the same location in Descending in **Fig.3**. This indicates that an uplift, accompanied by horizontal displacement to the west, has occurred on the south side of the epicentre of the upper plate. The amplitude of these ground deformations is about 20 cm, indicating that they are concentrated at the leading edge of the causative earthquake. This is consistent with the ground deformation of the inferred left lateral strike-slip fault.

5. COLLAPSE OF SIMPLE STRUCTURES

This earthquake caused extensive damage to buildings, which are mainly adobe structures. Many first story houses with an approximate height of 300-320 cm are enclosed by a 80 cm wide and 450 cm height wall. The failure mode of these simple one story houses fundamentally involved the toppling of walls perpendicular to the strike of the causative fault and shear failure of the walls perpendicular to the strike of the fault (**Fig.5**). In other words, the failure of these simple buildings was greately affected by the directivity of the strong motions.

The roof of the buildings was earthen supported by circular timber beams and roof load was carried by the walls. As the beam are placed on adobe walls, the shaking caused the fracture of walls by splitting action of the beams. Furthermore, most of the buildings has no lintels, which increase the integrity and ductility of the walls.

Fig.5 Views of the failed simple adobe buildings.

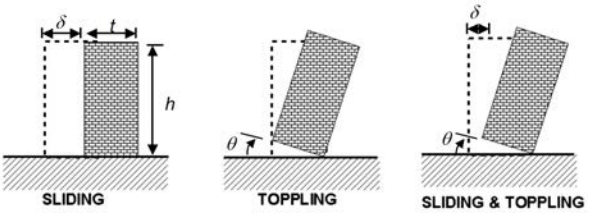

Fig.6 Failure modes of a wall.

6. INFERENCE OF MAXIMUM GROUND ACCELERATION AND VELOCITY

Aydan[4] summarized his earlier formulas to infer maximum ground acceleration and maximum ground velocity from the failed simple structures. The failure of these simple structures mainly involve toppling, sliding and combined sliding and toppling as ıllustrated in **Fig.6**. The conditions for different modes of failure shown in **Fig.6** derived for a horizontal maximum ground acceleration normalized by gravitational acceleration (simply known as horizonntal seismic coefficient) as follows

Toppling condition

$$\frac{a}{\mathrm{g}} > \frac{t}{h} \tag{1}$$

Sliding Condition

$$\frac{a}{\mathrm{g}} > \tan\phi \tag{2}$$

Toppling & Sliding Condition

$$\frac{a}{\mathrm{g}} > \frac{t}{h} \text{ and } \frac{a}{\mathrm{g}} > \tan\phi \tag{3}$$

Similarly, the maximum ground velocity may also be evaluated utilizing the displaced and/or toppled simple structures. This concept requires the equality of momentum to induce sliding, toppling or sliding and toppling to the imposed maximum kinetic energy associated with ground motions due to earthquakes. The final equations would take the following forms for the modes of sliding, toppling or sliding and toppling in terms of the block dimensions and the relative slip and/or rotation:

Toppling condition

$$v_{max} = \theta\sqrt{\mathrm{g}l} \tag{4}$$

Sliding Condition

$$v_{max} = \sqrt{2\mathrm{g}l\tan\phi} \tag{5}$$

Toppling & Sliding Condition

$$v_{max} = \sqrt{\mathrm{g}l(2\tan\phi + \theta^2)} \tag{6}$$

Where $l = \frac{1}{2}\sqrt{h^2 + t^2}$, $\theta = \frac{\pi}{4}\tan^{-1}\left(\frac{t}{h}\right)$,
ϕ: friction angle.

The friction anle for adobe bricks are generally within 30-40 degrees on the bases of past experiences.

7. EMPIRICAL METHOD TO ESTIMATE STRONG MOTIONS

There are many empirical attenuation relations for estimating ground motions in literature[5)-8)]. Including so-called next generation attenuation (NGA) relations, all these equations are essentially spherical or cylindrical attenuation relations and they cannot take into account the directivity effects. As it is shown in the beginning of this section, ground motions such as maximum ground acceleration ($A_{\max}$) and maximum ground velocity ($V_{\max}$) have strong directivity effects in relation to fault orientation. Furthermore, these relations are generally far below the maximum ground acceleration and they are incapable of obtaining the maximum ground acceleration ($A_{\max}$) or "peak ground acceleration (PGA)".

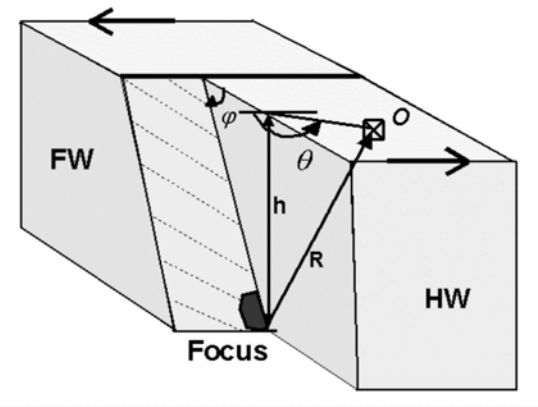

Fig.7 Illustration of geometrical fault parameters (R, θ, φ).

Table 2 Values of constants in Eq. (8) for inter-plate earthquakes.

	A	B(m/s)	D	E	F	G(Mw)
Amax	2.8	1000	0.5	1.5	0.5	1.05
Vmax	0.4	1000	0.5	1.5	0.5	1.05

Table 3 Values of constants in Eq. (8) for intra-plate earthquakes.

	A	B(m/s)	D	E	F	G(Mw)
Amax	2.8	1000	0.5	1.5	0.5	1.16
Vmax	0.4	1000	0.5	1.5	0.5	1.16

Table 4 Values of constants in Eq. (9) for earthquakes.

Faulting Type	a	b	c
Normal faulting	30	0.002	1.35
Strike-slip faulting	20	0.002	1.40
Thrust faulting	20	0.002	1.27

Aydan[9),10)] proposed an attenuation relation by combining their previous proposals together with the consideration of the inclination and length of earthquake fault using the following functional form (**Fig.7**):

$$\alpha_{max} = F_1(V_s) * F_2(R,\theta,\varphi,L^*) * F_3(M) \quad (7)$$

where V_s, θ, φ, L^* are the shear velocity of ground and the angle of the location from the strike and dip of the fault (measured anticlockwise with the consideration of the mobile side of the fault) and earthquake magnitude. The following specific forms of functions in Eq. (7) were put forward as

$$F_1(V_s) = Ae^{-V_s/B} \quad (8a)$$

$$F_2(R,\theta,\varphi,L^*) = e^{-R(1-D\sin\theta+E\sin^2\theta)(1+F\cos\varphi)/L^*} \quad (8b)$$

$$F_3(M) = e^{M/G} - 1 \quad (8c)$$

The same form is also used for estimating the maximum ground velocity (V_{max}). L^*(in km) is a parameter related to the half of the fault length. And it is related to the moment magnitude in the following form

$$L^* = a + be^{cM_w} \quad (9)$$

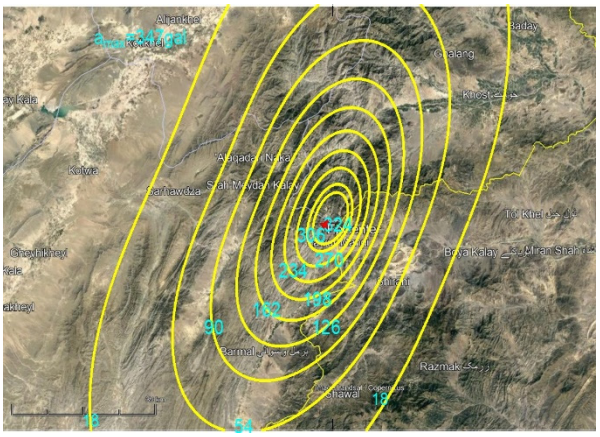

Fig.8 Maximum ground acceleration contours.

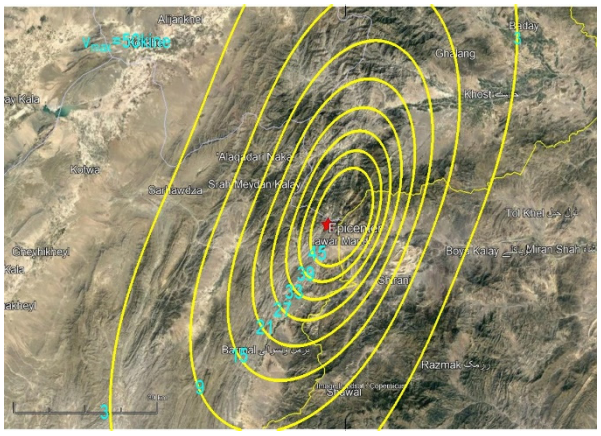

Fig.9 Maximum ground velocity contours.

The specific values of constants of Eqs. (8) and (9) for this earthquake are given in **Tables 2**, **3** and **4**.

These equations are utilized to infer the strong motions caused by the 2022 Paktika earthquake. **Figs.8** and **9** show the maximum ground acceleration and maximum ground velocity contours at the ground surface around the epicenter of the main shock, respectively.

8. FINITE ELEMENT METHOD TO ESTIMATE STRONG MOTIONS

Dynamic modelling is a method for dynamically evaluating the rupture propagation of a fault based on the balance of forces on the fault surface, and various methods have been proposed based on the difference method (FDM), finite element method (FEM), boundary element method (BEM), etc. These methods are characterised by their ability to reproduce the dynamic response of displacement and acceleration according to the linkage of adjacent faults, surface geometry and velocity layer structure through dynamic rupture propagation analysis of faults. Iwata et al.[11)-13)] used the three-dimensional finite element method (3DFEM) to investigate strong ground motions caused by several intraplate earthquakes in Japan. This method models the fault with joint elements and, based on the Mohr-Coulomb rupture criterion, the shear stress on the fault plane reaches a peak strength, which is reduced to a residual strength due to stress drop. By concentrating the stress on the asperities and rupturing some of them, the stress drop is distributed to the surrounding elements and the shear rupture spontaneously spreads to the surrounding faults.

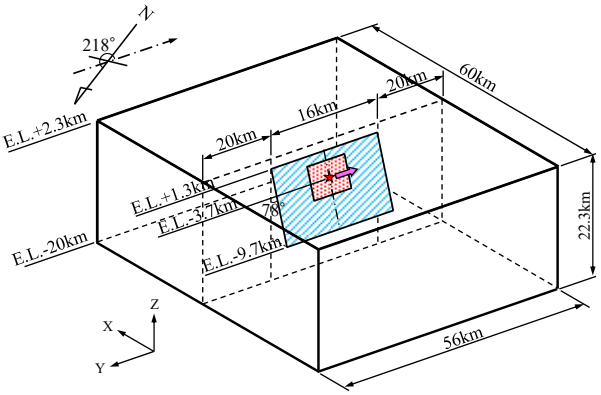

Fig.10 Schematic diagram of the analytical model and modelling of faults.

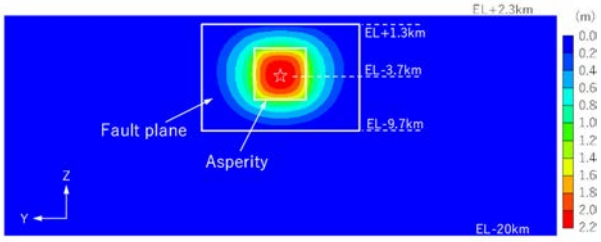

Fig.11 Slip at the final stage.

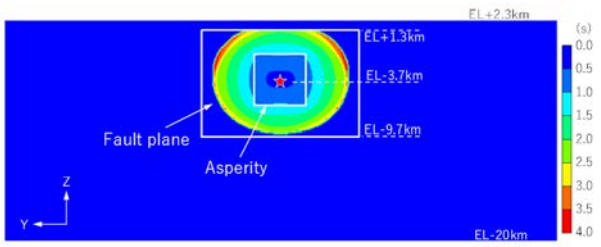

Fig.12 Slip propagation at different time steps.

Fig.10 shows a three-dimensional illustration of the earthquake fault and its surroundings for the 2022 Paktika earthquake. The ground was assumed to be homogeneous with Vs = 3.5 km/s and a fault plane with an inclination of 78°. Asperity size and stress drop were set in accordance with the strong-motion recipe by Irikura[14)]. The rupture initiation point was set at the centre of a 5.2 km x 5.2 km sperity at a depth of 6 km. The area is located in a mountainous region, with mountains exceeding 3000 m distributed on the west side of the fault. Therefore, calculations were carried out using a model that takes into account the flat ground surface and the actual topography.

The final slip distribution is shown in **Fig.11** and the distribution of slip times on the fault plane is shown in **Fig.12**. The rupture propagation velocity is 2.4 km/s, which is about 70% of the ground Vs and generally agrees with the general value. On the other hand, the maximum slip was of the order of 219 cm, approximately twice that estimated from empirical and finite fault models.

LOS displacement distribution maps of the analysed surface displacements in Sentinel-1 ascending and descending directions for the flat surface and actual topography are shown in **Figs.13** and **14**. Comparing these results with **Figs.3** and **4**, it can be seen that the calculated results, taking into account the actual topography, are remarkably similar to each other. However, it can be seen that the LOS displacements show little difference due to the topography of the ground surface.

Figs.15 and **16** show the calculated maximum ground acceleration and maximum ground velocity distributions for flat and actual terrain. As can be seen from **Fig.15** and **16**, the maximum ground acceleration and velocity are

similar for flat and actual terrain, but the distribution shape shows an amplification of the response along mountainous terrain when the topography is considered. Another important observation is that the effects of orientation and hanging/footwalls were clearly observed. As expected from the empirical method for estimating fault orientation and hanging and footwall effects, the seismic motions are larger and wider in the hanging wall sections than in the footwall sections. Furthermore, strong ground motions were found to be higher at the toe of the earthquake fault.

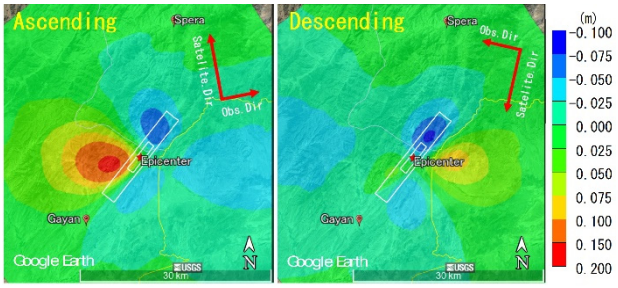

Fig.13 FEM results for LOS displacement with flat ground

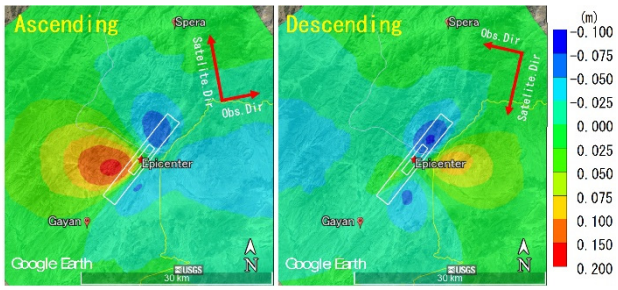

Fig.14 FEM results for LOS displacement for actual topography

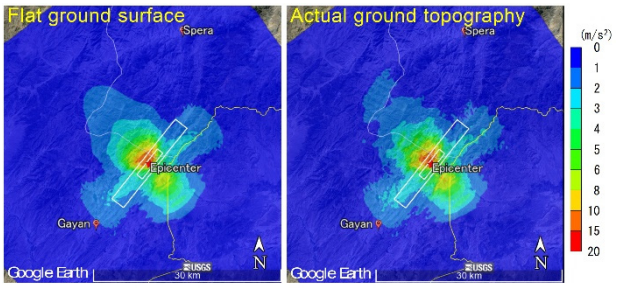

Fig.15 Comparison of FEM results for maximum ground acceleration with flat ground surface and actual ground topography

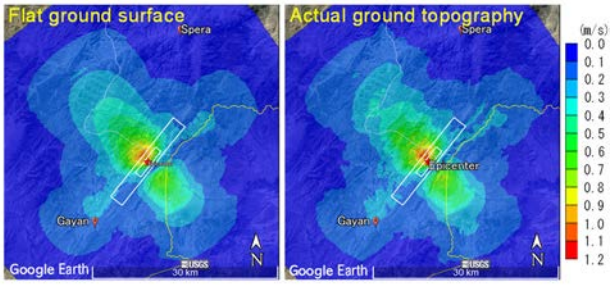

Fig.16 Comparison of FEM results for maximum ground velocity with flat ground surface and actual ground topography

9. FAULT RUPTURE MODELLING TECHNIQUES

There are many techniques subdividing a fault and fault planes in sub-fault elements to simulate broad-band as well as strong ground motions and they may be categorized sub-fault rupture techniques[15]. These techniques involve fault length and width, sub-fault size, seismic moment of fault, rupture pattern and rupture velocity , and propagation velocity of seismic waves. Techniques differ from each other in the way that how the effects of source, propagation path, radiation and site are modeled. For this purpose, stochastic, empirical and semi-empirical approaches utilized. One of the method is called the Empirical Green's function method was initially introduced by

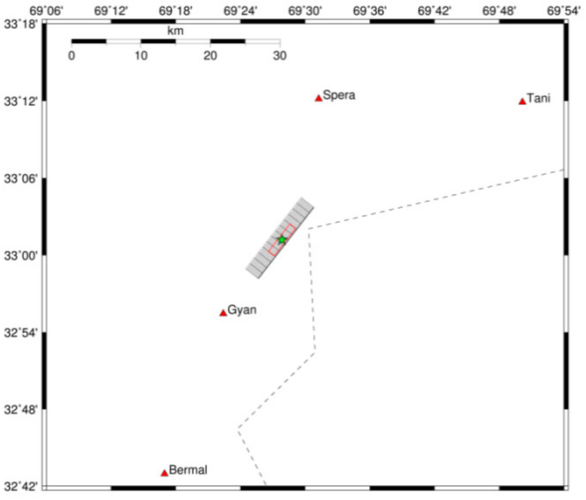

Fig.17 Mesh and selected locations

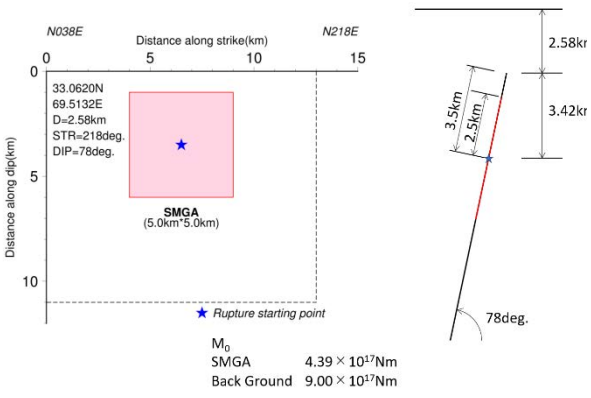

Fig.18 Fault model and its parameters

Hartzell[16]. Follow-up methods proposed Irikura[17] are modifications of Hartzell's method of summing empirical Green's functions. In empirical Green's function approach rupture propagation and radiation pattern were specified deterministically and the source propagation and radiation effects were included empirically by assuming that the motions observed from aftershocks contained this information[18]. Empirical Green's function method can be used only for a region where small events (i.e., aftershocks or foreshocks) of the target event are available.

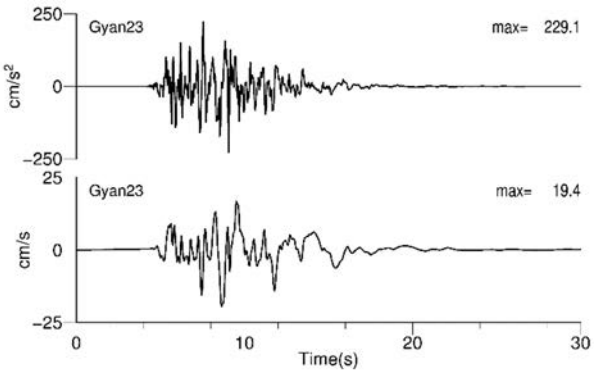

Fig.19 Computed acceleration and velocity responses in Gyan (scenario 23).

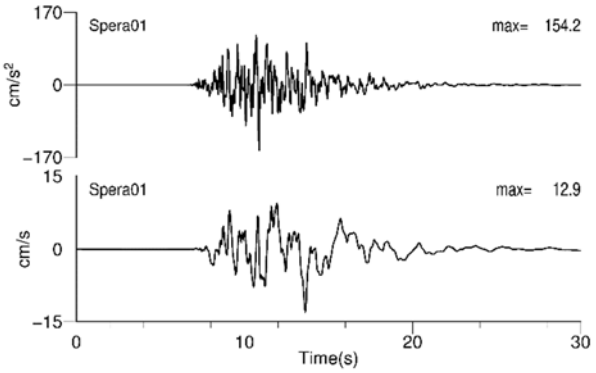

Fig.20 Computed acceleration and velocity responses in Spera (scenario 1).

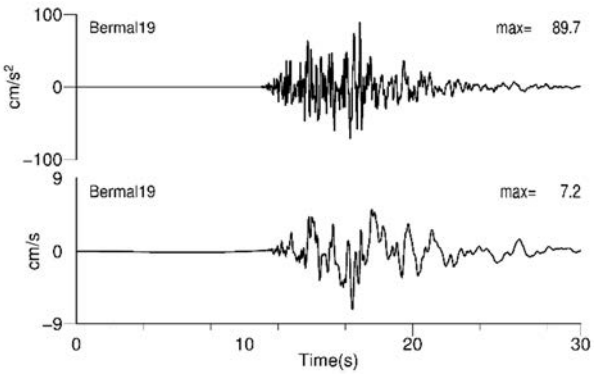

Fig.21 Computed acceleration and velocity responses in Bermal (scenario 19).

When records for small events are not available, the Strong Motion Prediction on Rock Surface by Superposed Evolutionary Spectra may also be used. The model incorporates the effect of direction of successive faulting relative to site using the superposing technique of evolutionary power spectra in time domain. This method for ground motion estimation was proposed by Sugito et al.[19] and named as Earthquake Motion Prediction Method (EMPR). This method is used to simulate the strong motion induced by the Paktika earthquake with a 16 km long and 10 km wide fault. The EMPR-II model of this method is utilized for simulating strong motions at three selected sites, namely, Spera, Giyan and Bermal in the earthquake affected area. **Figs.17** and **18** show the mesh and fault geometry, respectively. The fault was descritised into sub-fault domains and the location of the hypocenter was varied within the selected domain as shown in **Fig.17**.

Total 30 scenarios were considered and ground motions were computed for selected locations, namely, Spera, Gyan, Bermal and Tani. The damage and casualties were particularly heavy in Gyan, Spera and Bermal. **Figs.19, 20** and **21** show the computed acceleration and velocity responses in Gyan, Spera and Bermal. In the plots, the results for scenarios with larger ground accelerations were selected.

It should be noted, the computed ground velocity could be slightly less than those yielding higher ground velocity. The largest ground acceleration was observed in Gyan where the damage and casualties were the highest while the motions were less in Spera. The maximum ground acceleration was approximately 230 gals while the maximum ground velocity was less than 25 kines.

10. COMPARISONS OF STRONG MOTION ESTIMATIONS WITH INFERRED RESULTS

As there are no strong motion observation in the epicentral area, strong motions estimated from empirical methods and numerical methods are compared with those inferred from collapsed structure utilizing the procedure described in Section 6. **Figs.22** and **23** show the attenuation of maximum ground acceleration and velocity with distance together computed from the empirical method described in Section

7, inferred values from the failed simple structures using the method described in Section 6 and Sugito method.

As noted from **Figs.22** and **23**, the estimated values from the empirical method and Sugito Method are quite close to the inferred strong motions. Furthermore, it can be contemplated that the ground acceleration exceeding 100 gals was sufficient enough to cause the collapse of adobe structures in toppling mode (out-of-plane failure).

Although the estimations from 3F-FEM are not plotted in **Figs.22** and **23**, the maximum ground acceleration and velocity in the epicentral area (see **Figs.15** and **16**) are also quite similar to those obtained from the empirical method and the Sugito method as well as those inferred from collapsed simple adobe structures.

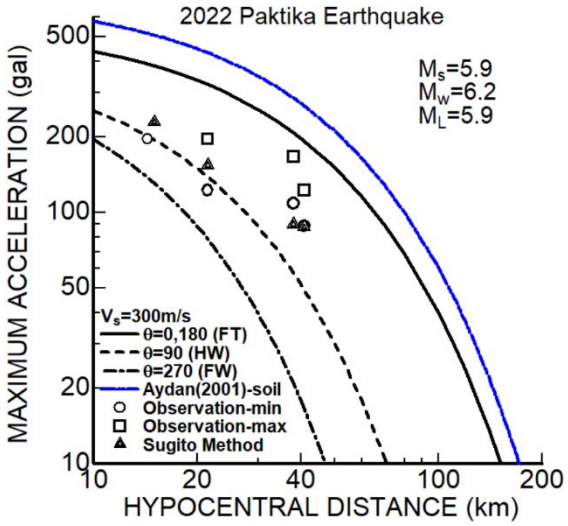

Fig.22 Comparison of estimations with inferred results.

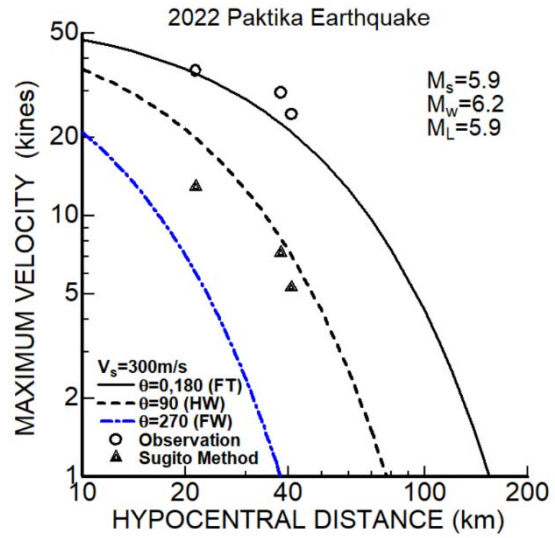

Fig.23 Comparison of estimations with inferred results.

11. CONCLUSIONS

The authors have attempted to evaluate strong motions associated with the 2022 Paktika earthquake using various techniques. As there is no strong motion data for this earthquake, the comparisons can only be done with those inferred from the collapsed simple adobe structures. The inferred maximum ground acceleration and velocity could be up to 250 gals and 45 kines. These estimations are quite close to those obtained from the empirical methods. The empirical method yielded that the maximum ground acceleration could be 347 gals while the maximum ground velocity is in the order of 50 kines.

3D-FEM analyses also indicated that the topography is an important factor for amplifying ground motions. Furthermore. 3D-FEM analyses could simulate the effects of the directivity and hanging wall/ foot wall on strong ground motions. Although computed results for strong motions are slightly larger, there is no doubt that better constitutive models would definetly yield better estimations results,

The DInSAR technique yielded permanent ground deformations up to 20 cm at the ground surface and displacement distribution is in accordance with those anticipated for sinistral strike-slip faulting. Similar to ground motions, the computational results from 3D-FEM analyses yielded that the consideration of the actual ground surface topography may yield results similar to those observed from DInSAR analyses.

The Superposed Evolutionary Spectra method developed by Sugito et al.[19] yielded quite similar results to those estimated from the empirical and 3D-FEM analyses and inferred strong ground motions from the collapse of simple adobe structures. Furthermore, the computational results clearly estimate why the damage and casualties were heavy in Gyan of Gayan District. The estimations also indicated that the maximum ground acceleration and ground velocity could be 230 gals and 25 kines.

REFERENCES

1) Nemati, M. : Seismotectonic and seismicity of Makran, a bimodal subduction zone, SE Iran. *Journal of Asian Earth Sciences* 169, pp.139-161, 2018.
2) USGS: M 5.9 – 46 km SW of Khōst, Afghanistan, 2022, *https://earthquake.usgs.gov/earthquakes/eventpage/us7000hj3u/finite-fault*
3) Harvard CMT Catalog 2022 : *Global Centroid Moment Tensor*, 22 June 2022, Archieved from the original on 23 June 2022.

4) Aydan, Ö. : *Earthquake Science and Engineering*, CRC Press, Taylor and Francis, 496p., 2022.
5) Joyner, W.B. and Boore, D.M. : Peak horizontal acceleration and velocity from strong motion records from the 1979 Imperial Valley California Earthquake. *Bull. Seis. Soc. Am.*, 71(6), pp.2011-2038, 1981.
6) Campbell, K.W. : Near source attenuation of peak horizontal acceleration. *Bull. Seis. Soc. Am.*, 71(6), pp.2039-2070, 1981.
7) Ambraseys, N.N. : Engineering Seismology. *Earthquake Engineering and Structural Dynamics*, V.17,pp.1-105, 1988.
8) Aydan, Ö., Sezaki, M. and Yarar, R. : The seismic characteristics of Turkish Earthquakes. *The 11th World Conf. on Earthquake Eng.*, CD-2, Paper No:1270, 1996.
9) Aydan, Ö. 2007. The inference of seismic and strong motion characteristics of earthquakes from faults with a particular emphasis on Turkish earthquakes. The 6th National Earthquake Engineering Conference of Turkey, Istanbul, 563-574.
10) Aydan, Ö. : Ground motions and deformations associated with earthquake faulting and their effects on the safety of engineering structures, *Encyclopedia of Sustainability Science and Technology*, Springer, R. Meyers (Ed.) pp.3233-3253. 2012.
11) Iwata, N., Adachi, K., Takahashi, Y., Aydan, Ö., Tokashiki, N. and Miura, F. : Fault rupture simulation of the 2014 Kamishiro Fault Nagano Prefecture Earthquake using 2D and 3D-FEM. *EUROCK2016*, Ürgüp, pp.803-808, 2016.
12) Iwata, N., Kiyota, R., and Aydan, Ö. : 3D Strong Motion Simulation of the 1984 Western Nagano Prefecture Earthquake and its implication on Ontake Volcano landslide. *Proc. of the 16th inter. conf. of IACMAG, Vol.2*, pp.613-620, 2021.
13) Iwata, N., Otsuka, Y., Aydan, Ö., Ito, T., Sainoki, A. and Ikeda, T. : Analytical study on the effect of damage zones on the occurrence of surface rupture at the Hinagu fault, *Rocdyn-4*, 2022(in press).
14) Irikura, K. : Predicting strong ground motions with "Recipe", *Bull. Earthq. Res. Inst. Univ. Tokyo*, 81, pp.341-352, 2006.
15) IAEA (International Atomic Energy Agency) : Ground motionsimulation based on fault rupture modelling for seismic hazard assessment in site evaluation for nuclear installation, *IAEA Safety Report Series, N*o.85, 126p., 2015.
16) Hartzell, S.H. : Earthquake aftershocks as Green's functions. *Geophys. Res. Lett.* 5, pp.1-4, 1978.
17) Irikura, K. : Semi-empirical estimation of strong ground motions during large earthquakes. *Bull. Disaster Prev. Res. Inst.* (Kyoto University) 33, pp.63-104, 1983.
18) Somerville, P.G., Sen, M. and Cohee, B. : Simulation of strong ground motion recorded during the 1985 Michoacan, Mexico an Valparaiso, Chile earthquakes. *Bull. Seismol. Soc. Am.* 81, pp.1- 27, 1991.
19) Sugito,M., Furumoto,Y. and Sugiyama, T. : Strong Motion Prediction on Rock Surface by Superposed Evolutionary Spectra, *12th World Conference on Earthquake Engineering*, 2111/4/A, CD-ROM, 2000.

(Received September 6, 2022)
(Accepted ?? ??, ????)